ADVANCED MATERIALS
www.advmat.de

Manipulating the Mixed-Perovskite Crystallization Pathway Unveiled by In Situ GIWAXS

*Minchao Qin, Kinfai Tse, Tsz-Ki Lau, Yuhao Li, Chun-Jen Su, Guang Yang, Jiehuan Chen, Junyi Zhu, U-Ser Jeng, Gang Li, Hongzheng Chen, and Xinhui Lu**

Mixed perovskites have achieved substantial successes in boosting solar cell efficiency, but the complicated perovskite crystal formation pathway remains mysterious. Here, the detailed crystallization process of mixed perovskites ($FA_{0.83}MA_{0.17}Pb(I_{0.83}Br_{0.17})_3$) during spin-coating is revealed by in situ grazing-incidence wide-angle X-ray scattering measurements, and three phase-formation stages are identified: I) precursor solution; II) hexagonal δ-phase (2H); and III) complex phases including hexagonal polytypes (4H, 6H), MAI–PbI_2–DMSO intermediate phases, and perovskite α-phase. The correlated device performance and ex situ characterizations suggest the existence of an "annealing window" covering the duration of stage II. The spin-coated film should be annealed within the annealing window to avoid the formation of hexagonal polytypes during the perovskite crystallization process, thus achieving a good device performance. Remarkably, the crystallization pathway can be manipulated by incorporating Cs^+ ions in mixed perovskites. Combined with density functional theory calculations, the perovskite system with sufficient Cs^+ will bypass the formation of secondary phases in stage III by promoting the formation of α-phase both kinetically and thermodynamically, thereby significantly extending the annealing window. This study provides underlying reasons of the time sensitivity of fabricating mixed-perovskite devices and insightful guidelines for manipulating the perovskite crystallization pathways toward higher performance.

Metal-halide perovskites, with a general formula of ABX_3 (e.g., A = methylammonium (MA^+), formamidinium (FA^+), Cs^+; B = Pb^{2+}, Sn^{2+}; X = I^-, Br^-, Cl^-), have demonstrated great potential in optoelectronic applications, such as light emitting diodes[1] and solar cells.[2] The power conversion efficiency (PCE) of perovskite solar cells (PSCs) has been rapidly pushed above 23% in recent several years, mainly owing to the huge freedom in compositional engineering of mixed perovskites.[3,4] On the other hand, complex composition of perovskite challenges the fundamental understanding of the crystallization mechanism, which is closely coupled with the device performance and reproducibility.

During the crystal formation of perovskite films, numerous secondary phases have been observed, accompanied with or substituting the desired perovskite black phase (cubic/tetragonal α-phase). The most commonly reported secondary phase is the yellow δ-phase. To predict the formation of favored crystal structures, one can use the empirical Goldschmidt tolerance factor $t = (r_A + r_X)/\sqrt{2}(r_B + r_X)$, where $r_{A,B,X}$ are the ionic radii of the corresponding components in the perovskite formula.[5] Perovskite with a t factor in the range of 0.8–1.0, for instance $MAPbI_3$, is ideal to form α-phase.[6] $FAPbI_3$, with the relatively bulkier FA^+ cation thus a t factor approaching the up-limit of the α-phase range, was reported to form either hexagonal δ-phase (2H) or α-phase depending on the processing conditions.[7] In contrast, all-inorganic perovskite $CsPbI_3$ with a too small t due to the much smaller Cs^+ cation tends to form orthorhombic δ-phase at room temperature.[8] Therefore, the mixed FA/MA, FA/Cs or triple-cation systems were found to exhibit better structural stability due to

M. Qin, K. Tse, Dr. T.-K. Lau, Y. Li, Prof. J. Zhu, Prof. X. Lu
Department of Physics
The Chinese University of Hong Kong
Shatin 999077, Hong Kong
E-mail: xhlu@phy.cuhk.edu.hk
Dr. C.-J. Su, Dr. U.-S. Jeng
National Synchrotron Radiation Research Center
Hsinchu Science Park
Hsinchu 30076, Taiwan
The ORCID identification number(s) for the author(s) of this article can be found under https://doi.org/10.1002/adma.201901284.

DOI: 10.1002/adma.201901284

G. Yang, Prof. G. Li
Department of Electronic and Information Engineering
The Hong Kong Polytechnic University
Kowloon 999077, Hong Kong
J. Chen, Prof. H. Chen
State Key Laboratory of Silicon Materials
MOE Key Laboratory of Macromolecular Synthesis and Functionalization
Department of Polymer Science and Engineering
Zhejiang University
Hangzhou 310027, P. R. China
Dr. U.-S. Jeng
Department of Chemical Engineering
National Tsing Hua University
Hsinchu 30013, Taiwan

 © 2019 WILEY-VCH Verlag GmbH & Co. KGaA, Weinheim

a balanced tolerance factor.[9–11] Regarding halide ions, Br^- ion is often integrated into I^--based perovskite systems for the purpose of tuning the bandgap. On the other hand, it also slightly increases the tolerance factor due to its smaller ionic size compared with that of I^-. Consequently, several studies have successfully demonstrated the low-temperature formation of α-phase $CsPbI_{3-x}Br_x$,[12] owing to the Br^- correction to the tolerance factor. In contrast, for FA^+ dominant lead iodide systems which already have a relatively high t, the addition of Br^- might cause unwanted halide phase segregation[10] and hexagonal polytypes.[13]

Besides structural phase stability, controlling the crystal growth kinetics is another key to yield high-quality perovskite films. Recently, researchers have noticed the time sensitivity in fabricating high-performance mixed-perovskite devices, however, at an empirical level.[14] To elucidate the time-resolved film formation mechanism, in situ characterization techniques, such as in situ grazing-incidence wide-angle X-ray scattering (GIWAXS), are usually employed. Generally, a perovskite film is fabricated through two major steps: forming an as-cast film and thermal annealing. Many in situ studies were focused on the thermal annealing step.[15–17] For instance, Gratia et al. identified hexagonal polytypes (6H and 4H) for mixed-ion perovskites during the annealing process.[13] Pool et al. optimized thermal annealing time and temperature for $FAPbI_3$ perovskite films based on in situ GIWAXS measurements.[16] Alsari et al. introduced an interdigitated back-contact structure to in situ monitor the device performance upon thermal annealing.[17] There are very limited studies on film formation from the solution stage. Munir et al. investigated the solidification pathway of MA^+-based perovskites during spin-coating process and found that precursor solvates could impact the morphology of the perovskite film.[18] The influence of other fabrication techniques, such as slot die[19] and blade coating[20] was also reported. However, most of these studies focused on the single-cation (MA- or FA-based) and single-halide (I- or Br-based) systems. The film formation process of mixed-cation systems, which is expected to involve complicated phase behavior and crystallization kinetics, remains unclear during the initial spinning process.

Here, we investigate in detail the crystallization process of a prototypical high-performance mixed-perovskite system $Cs_x(FA_{0.83}MA_{0.17})_{1-x}Pb(I_{0.83}Br_{0.17})_3$[10,21] and the role of Cs^+ ions in altering the phase formation pathways. Synchrotron-based in situ GIWAXS measurements are performed throughout the whole spin-coating process (**Figure 1**). For the system without Cs^+, three stages of film growth are identified: I) precursor solution; II) hexagonal δ-phase (2H); and III) complex phases including hexagonal polytypes (4H, 6H), MAI–PbI_2–DMSO intermediate phases, and perovskite α-phase. Surprisingly, the system with Cs^+ undergoes only the first two stages. The perovskite α-phase appears as early as stage II. In accordance with device results, we propose the concept of "annealing window," which spans the duration of stage II. If the thermal annealing is performed within the annealing window, a high-quality perovskite film can be attained, thus leading to good device performance. Otherwise, a low-quality perovskite film is formed with the residual of unwanted secondary phases. The unique role of Cs^+ here is to facilitate the formation of perovskite phase, thereby suppressing the formation of secondary phases. Consequently, the annealing window is significantly extended. Our findings are further supported by ex situ characterizations such as X-ray diffraction (XRD), absorption spectra, scanning electron microscopy (SEM) as well as density functional theory (DFT) calculations. In brief, this work reveals a detailed time-resolved crystallization process of mixed perovskites and the existence of "annealing window." It provides underlying reasons of the time sensitivity of fabricating high-performance mixed-perovskite films and insightful guidelines for further perovskite compositional engineering toward higher performance and reproducibility.

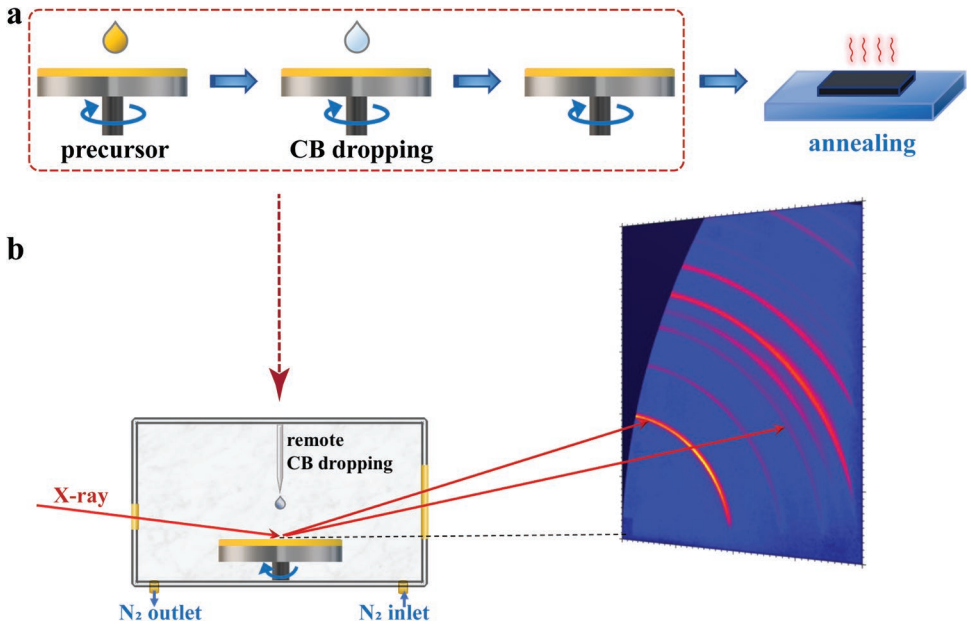

Figure 1. Schematics of the film fabrication procedure and the experimental setup for in situ GIWAXS characterization. a) The basic steps of perovskite fabrication process. b) The in situ GIWAXS sample chamber equipped with a spin coater, an antisolvent syringe under nitrogen environment.

© 2019 WILEY-VCH Verlag GmbH & Co. KGaA, Weinheim

The in situ GIWAXS measurements were performed on beamline 23A at the National Synchrotron Radiation Research Center (NSRRC), Hsinchu, Taiwan.[22] To achieve high device performance with the mixed-perovskite system, the so-called "one-step antisolvent" fabrication process is often employed (Figure 1a) to grow a uniform and compact perovskite film.[23,24] Here, we focus on the perovskite crystallization process during the whole spin-coating process before annealing (highlighted in the dashed rectangle). The acquirement of 2D GIWAXS patterns (3 s per frame) is launched with the dropping of precursor solution and lasts for 300 s until the scattering patterns are nearly unchanged (Figure 1b). To capture the whole crystallization process during spinning, the spin speed is slowed down to 1500 rpm and the antisolvent chlorobenzene (CB) is injected onto the film at the 50th second. The perovskite films exhibit isotropic scattering rings, indicating no preferential orientation with respect to the substrate.[25] Therefore, we utilize a relatively high incident angle of 2° for a better peak resolution and extract intensity profiles along the q_z direction to examine the crystallization process in detail.

We first investigate the crystallization process of mixed-perovskite systems without Cs^+ ($FA_{0.83}MA_{0.17}Pb(I_{0.83}Br_{0.17})_3$). Representative 2D GIWAXS patterns at different crystallization stages are shown in **Figure 2**a–d with the corresponding intensity profiles displayed in Figure 2i. A typical scattering pattern measured at the beginning of the spin-coating process is presented in Figure 2a. The broad and weak scattering ring at $q \approx 0.50$ Å^{-1} originates from the precursor solution, consistent with previous reports.[18] Note here, the three sharp scattering rings at $q \approx 1.9$, 2.3, and 2.6 Å^{-1} come from the FTO substrates, confirming the probing of the bulk film structure with an incident angle of 2°. Figure 2b shows the scattering pattern captured right after the CB dropping. The precursor scattering ring disappears, followed by the appearance of a broad scattering ring from CB at $q \approx 1.3$ Å^{-1}, which also disappears quickly due to the fast evaporation of CB. Concomitantly, a sharp yellow δ-phase peak (hexagonal 2H) emerges at $q \approx 0.84$ Å^{-1}[26] and is gradually strengthened upon spinning (Figure 2c). After certain spinning time, several distinct crystalline phases are established, suggested by the presence of a few scattering rings in Figure 2d. As depicted in Figure 2i (orange curve), these peaks are indexed as perovskite phase (1.0 Å^{-1}),[19] MAI–PbI_2–DMSO intermediate phases (0.47, 0.51, and 0.65 Å^{-1}),[24,27] and hexagonal 4H (0.83 and 0.93 Å^{-1}) and 6H (0.87 Å^{-1}).[13] The crystal structures of cubic perovskite, hexagonal polytypes 2H, 4H and 6H, and MAI–PbI_2–DMSO intermediate phases are illustrated in Figure S1 (Supporting Information).

Surprisingly, the mixed perovskites with 10% Cs^+ (i.e., $Cs_{0.1}(FA_{0.83}MA_{0.17})_{0.9}Pb(I_{0.83}Br_{0.17})_3$) demonstrate a notably distinct crystallization process. In stage I, the precursor ring is observed at $q \approx 0.50$ Å^{-1}, similar to the control system without Cs^+ (Figure 2e). After the trigger of CB dropping (Figure 2f) to enter stage II (Figure 2g,h), the peak of the hexagonal 2H phase is significantly diminished, while the peaks of complex secondary phases observed in stage III of the control system are no longer detected. Instead, the perovskite α-phase is quickly built up upon spinning (green and orange curves in Figure 2j). The findings suggest that Cs^+ could facilitate the formation of perovskite phase and simultaneously suppress other secondary phases. As summarized in the schematic of time axis (blue arrow in Figure 2), there exist three stages during the crystallization of the mixed-perovskite film without Cs^+—stage I: precursor solution; stage II: 2H phase; stage III: complex phases including hexagonal polytypes (4H, 6H), MAI–PbI_2–DMSO

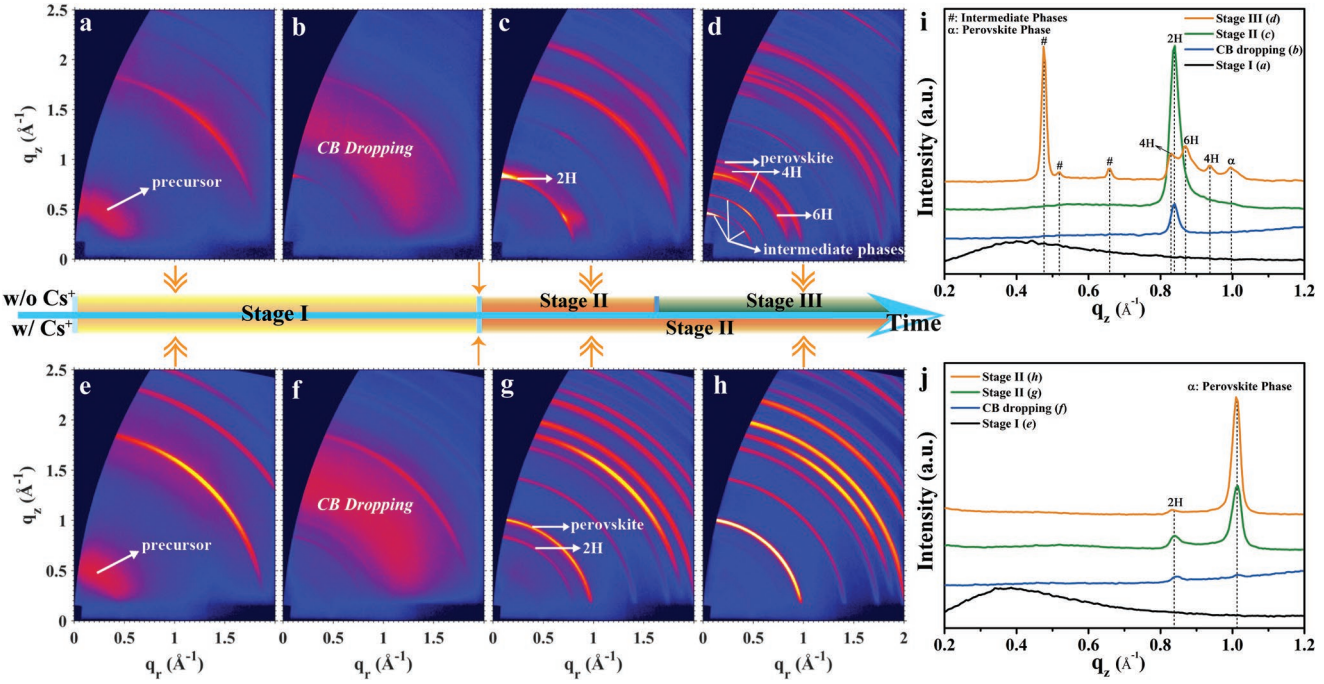

Figure 2. Different crystallization stages versus spinning time for perovskite formations without and with Cs^+. a–h) 2D GIWAXS patterns at different crystallization stages for films without Cs^+ (a–d) and with 10% Cs^+ (e–h). i,j) The intensity profiles along the q_z direction for films without Cs^+ (i) and with 10% Cs^+ (j).

© 2019 WILEY-VCH Verlag GmbH & Co. KGaA, Weinheim

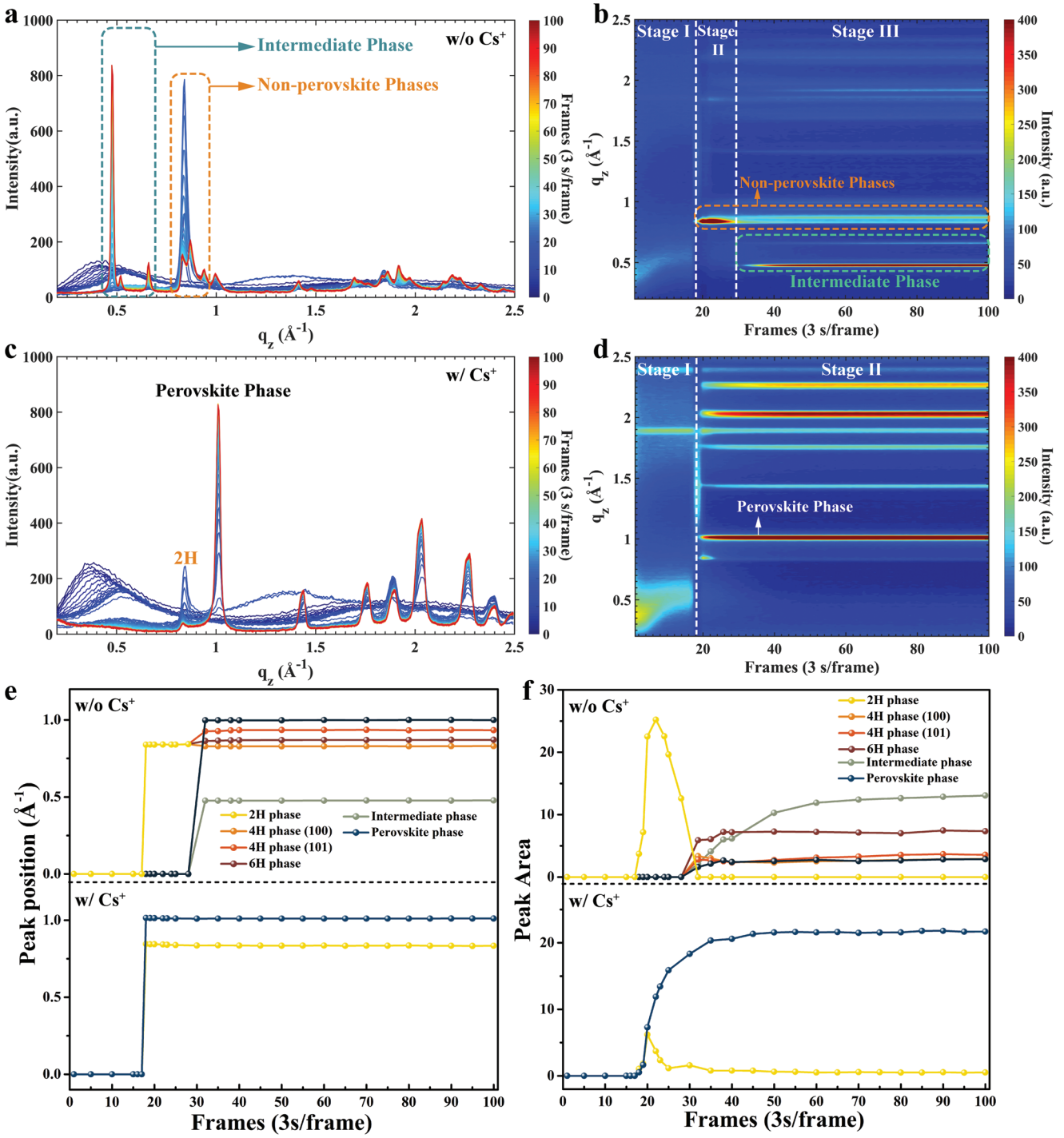

Figure 3. Time-resolved GIWAXS profile analysis. a,c) The GIWAXS intensity profiles along the q_z direction measured for 100 frames (3 s per frame) for perovskites without Cs^+ (a) and with 10% Cs^+ (c), and b,d) the false-color intensity maps versus q_z and frames without Cs^+ (b) and with 10% Cs^+ (d). e,f) The corresponding time evolutions of peak positions (e) and peak areas (f) for nonperovskite, intermediate, and perovskite phases as a function of frames.

intermediate phases, and perovskite α-phase. In contrast, the mixed perovskite with Cs^+ experiences only two stages—stage I: precursor solution; stage II: 2H and perovskite α-phase.

To understand the time evolution of the crystallization process during the spin-coating, we summarize the in situ GIWAXS intensity profiles of perovskites without and with Cs^+ in **Figure 3**a,c and plot the false-color intensity map versus the wave vector q_z (x-axis) and the frame numbers (y-axis, 3 s per frame) in Figure 3b,d. The corresponding time evolutions of peak positions and peak areas are shown in Figure 3e,f. For both perovskites without and with Cs^+, the scattering behaviors in stage I are similar: the precursor peak position shifts from 0.40 to

© 2019 WILEY-VCH Verlag GmbH & Co. KGaA, Weinheim

0.50 Å^{-1} due to the removal of DMF molecules during the spinning.[19] The CB dropping triggers the crystallization of precursor solutions at the 17th frame. Subsequently, perovskites without and with Cs^+ undergo totally different crystallization pathways, as discussed in detail in the following. It is noteworthy that we also conducted in situ GIWAXS measurements for mixed perovskites without Cs^+ under other different CB dropping time such as the 5th, 25th, and 100th s, as shown in Figures S2 and S3 (Supporting Information). Similar crystallization processes were observed regardless of different CB dropping time, indicating that the crystallization process of mixed perovskites is insensitive to the CB dropping time as long as the precursor solution is not totally dried out. In short, the timing of CB dropping merely changes the boundary between stages I and II, but not the phase formation pathway.

For the perovskite without Cs^+ (Figure 3b), stage II lasts for about 10 frames (from the 18th to the 28th frame, ≈30 s). The hexagonal 2H phase (0.84 Å^{-1}) is the only crystalline phase observed during stage II, which reaches maximum population at the 23th frame. The system enters stage III at the 29th frame, when the 2H peak splits into four peaks, originated from hexagonal 4H (0.83, 0.93 Å^{-1}), hexagonal 6H (0.87 Å^{-1}) and cubic/tetragonal perovskite (1.0 Å^{-1}), respectively. Nearly simultaneously, scattering peaks emerge at q = 0.47, 0.51, and 0.65 Å^{-1}, corresponding to the MAI–PbI_2–DMSO intermediate phases. The time evolution of each phase in terms of peak position and area is shown in Figure 3e,f. Note that the peaks at 0.47 and 0.83 Å^{-1} are chosen to represent the intermediate and 4H phases, respectively. In Figure 3f, it is evident that the peak area of 2H phase, corresponding to its crystalline domain population, quickly decreases to zero in accordance with a fast increase of 4H, 6H and perovskite α-phases to stable values around the 40th frame, indicating the experience of phase transitions. In contrast, the peak area of the intermediate phase slowly increases until around the 80th frame, exhibiting a slower formation process of MAI–PbI_2–DMSO intermediate phase.[27] For the perovskite with 10% Cs^+, the crystallization process is much simpler: both peaks of 2H and perovskite phases appear right after the CB dropping (stage II). The peak area of 2H phase maximizes at the 22th frame and then drops to zero at the 32th frame. The peak area of perovskite phase keeps increasing until the 50th frame and then remains stable. These results suggest that Cs^+ plays a critical role in altering the film crystallization pathway not only thermodynamically but also kinetically: the system with Cs^+ effectively bypasses the formation of unwanted secondary phases (stage III) and yields the desired perovskite crystallites at much earlier time.

To correlate the diverse crystal formation pathways of perovskite films without or with Cs^+ with the device performance, we fabricated $Cs_x(FA_{0.83}MA_{0.17})_{1-x}Pb(I_{0.83}Br_{0.17})_3$ (x = 0 or 0.1) based PSCs using the one-step antisolvent process annealed at 100 °C for 60 min with different spinning times (0, 15, 30, and 100 s) after the CB dropping. The device structure is FTO/SnO_2/mixed perovskite/Spiro-OMeTAD/Au (Figure S4a, Supporting Information). The J–V curves and parameters of typical PSCs are shown in Figure S4b,c and Table S1 (Supporting Information). For PSCs without Cs^+ (**Figure 4**a), decent device characteristics can be achieved for the films annealed at both

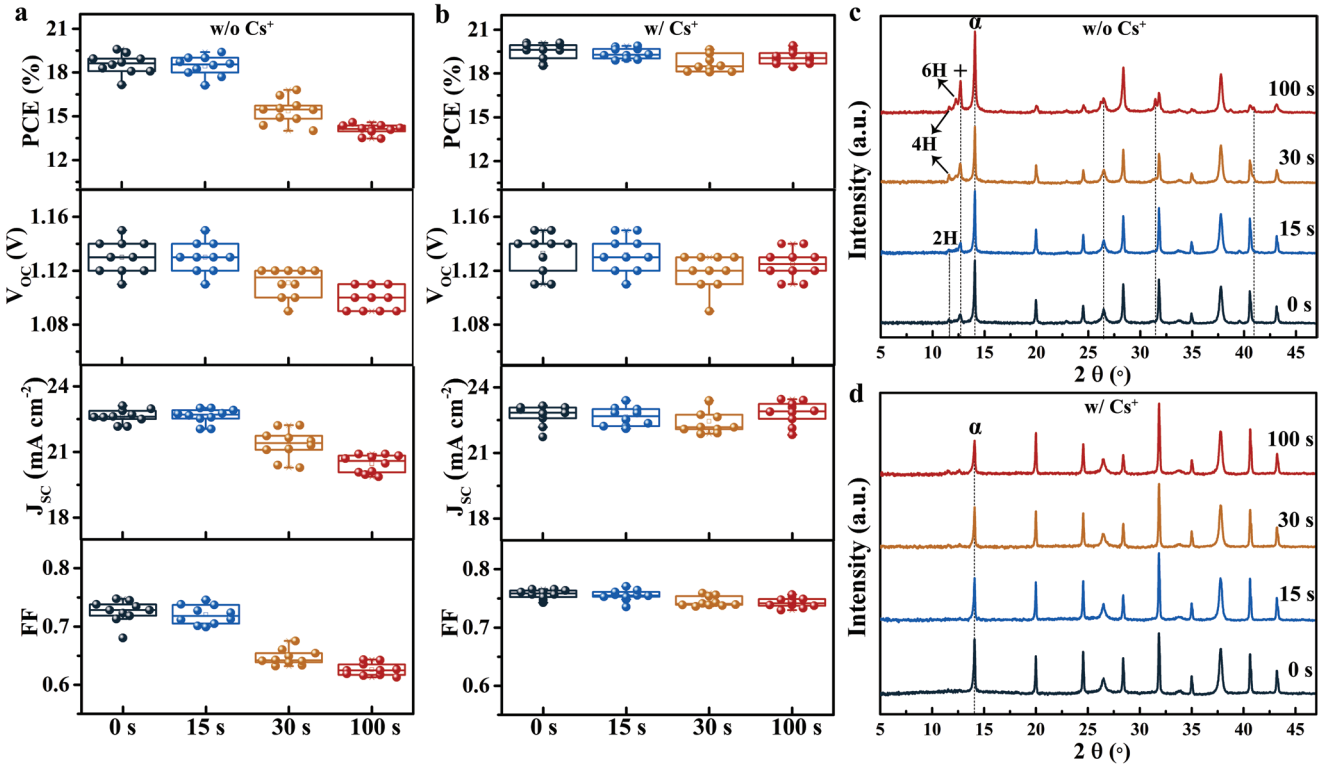

Figure 4. Device performance and ex situ XRD characterization. a,b) Statistical device performance of PSCs based on the perovskite films without Cs^+ (a) and with 10% Cs^+ (b), annealed with different spinning time (0, 15, 30, and 100 s) after the CB dropping. c,d) Ex situ XRD results for the corresponding perovskite films without Cs^+ (c) and with 10% Cs^+ (d). α and + denote the identified peaks of α-phase and PbI_2, respectively.

© 2019 WILEY-VCH Verlag GmbH & Co. KGaA, Weinheim

0 and 15 s. However, obvious device degradation is observed for films annealed with longer spinning time (30 and 100 s). In other words, the as-cast film is required to be annealed shortly after CB dropping and a delay of annealing will result in poor device performance. On the contrary, the PSCs with 10% Cs^+ could achieve good performance regardless of spinning time (Figure 4b). Combining with in situ crystallization results, we posit that there exists an "annealing window," spanning the duration of stage II. For the perovskite film without Cs^+ which undergoes three stages in the crystallization process, it is essential to anneal the film within the short period of stage II before entering stage III. For the perovskite film with Cs^+ which only experiences two stages, the annealing window is significantly extended, reducing the time sensitivity of performing the annealing step to obtain a high-performance device.

The corresponding X-ray diffraction spectra of perovskite films annealed with different spinning times (0, 15, 30, and 100 s) after the CB dropping are presented in Figure 4c,d. For perovskite films without Cs^+ annealed within the annealing window (0 and 15 s), the XRD patterns exhibit a typical perovskite α-phase peak at 14.1° along with tiny secondary peaks at 11.7° and 12.7°, associated with the 2H and PbI_2 phases.[11] In the course of in situ GIWAXS results, it implies that thermal annealing could promote the phase transition from 2H to α-phase, accompanied by the formation of PbI_2.[19] In contrast, the perovskite films without Cs^+ annealed beyond the annealing window (30 and 100 s) show additional secondary peaks at 11.6°, 12.2°, 26.2°, 31.5°, and 40.9°, which can be assigned to 4H and 6H phases.[13] Furthermore, the PbI_2 peak at 12.7° is strengthened with more spinning time. Together, it suggests that annealing the film with complex secondary phases formed in stage III will lead to the residual of hexagonal phases and more excessive PbI_2. Further evidences of the existence of these undesirable phases in the annealed films can be recognized in the absorption spectra (Figure S5a, Supporting Information) and SEM images (Figure S6, Supporting Information). For films without Cs^+ annealed outside the annealing window, extra absorption edges between 500 and 600 nm associated with hexagonal phases are observed. Obvious PbI_2 crystals can be identified in SEM images, which are reported to be detrimental to the device performance.[28] It is worth noting that MAI–PbI_2–DMSO intermediate phases at q = 0.47, 0.51, and 0.65 $Å^{-1}$ (2θ of 6.6°, 7.2°, and 9.2°) observed in GIWAXS patterns all disappear after annealing. Remarkably, with 10% Cs^+, the perovskite films fabricated with different spinning time exhibit consistent XRD patterns (Figure 4d), absorption spectra (Figure S5b, Supporting Information), and

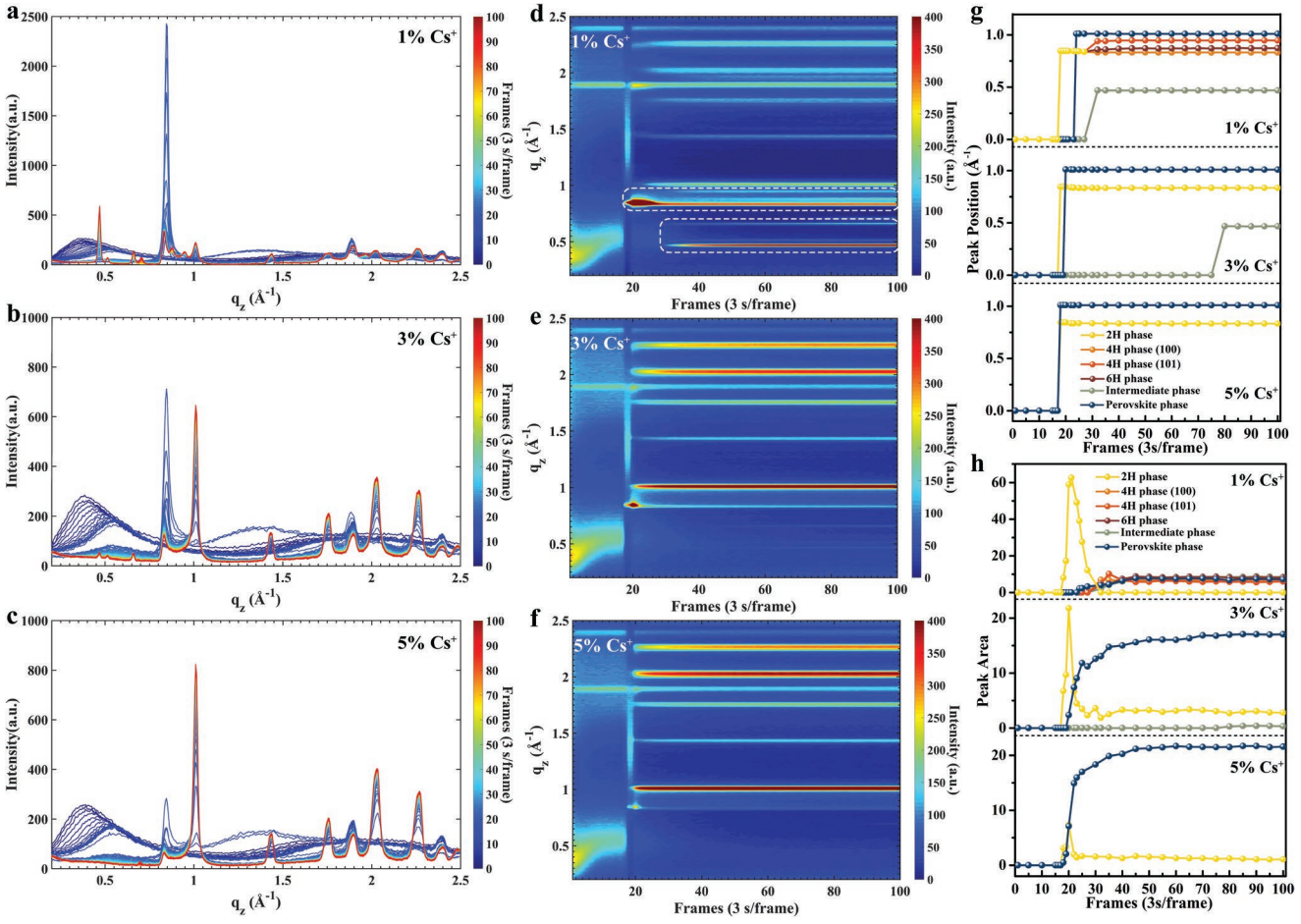

Figure 5. In situ GIWAXS measurements with different Cs^+ concentrations. a–c) The GIWAXS intensity profiles along the q_z direction for perovskites with 1% Cs^+ (a), 3% Cs^+ (b), and 5% Cs^+ (c), and d–f) false-color intensity maps versus q_z and frame numbers for perovskites with 1% Cs^+ (d), 3% Cs^+ (e), and 5% Cs^+ (f). g,h) The corresponding time evolutions of peak positions (g) and peak areas (h) for nonperovskite, intermediate, and perovskite phases as a function of frame numbers.

© 2019 WILEY-VCH Verlag GmbH & Co. KGaA, Weinheim

SEM images (Figure S7, Supporting Information), signifying the formation of pure α-phase and good quality perovskite films.

To elucidate the impact of Cs^+ in the crystallization process of mixed perovskites, we carried out in situ GIWAXS measurements with different Cs^+ concentrations. The GIWAXS intensity profiles are summarized in **Figure 5**a–c for perovskites with 1%, 3%, and 5% Cs^+, and the corresponding false-color intensity maps versus q_z and frame numbers are shown in Figure 5d–f. With a low Cs^+ concentration of 1%, the perovskite film also undergoes three crystallization stages during the spinning operation, similar to that observed in the film without Cs^+: precursor solution (stage I), 2H phase (stage II), and complex phases (stage III); but note that the perovskite phase emerges slightly earlier, at the ≈24th frame (Figure 5g,h). When the Cs^+ concentration increases to 3%, the 4H and 6H phases are already suppressed while the 2H and perovskite phases remain in the whole spinning operation. Consistently, the perovskite phase emerges even earlier at ≈20th frame with a higher peak intensity. Compared with the 10% Cs^+ case (Figure 3e), the scattering peak of the intermediate phase of the 3% Cs^+ film still emerges but with a longer spinning time (≈the 80th frame) and a much lower peak intensity. When the Cs^+ concentration further increases to 5%, the crystallization process is nearly identical to the 10% case. The perovskites with higher Cs^+ concentrations such as 15% also undergo two crystallization stages, as shown in Figure S8 (Supporting Information). These results further confirm that incorporating Cs^+ (>5%) could prominently expediate the formation of mixed perovskite α-phase, therefore suppressing other unwanted phase transition pathways. Noted that the receipt we employed contains 10 mol% excess of PbI_2/$PbBr_2$.[4] It is possible that the added Cs^+ ions react with the excessive PbI_2/$PbBr_2$ to form $CsPbI_xBr_{3-x}$ and in turn eliminate the secondary phase in the perovskite film. However, there is no obvious evidence of the formation of $CsPbI_xBr_{3-x}$ either cubic or yellow phases based on the diffraction results. When the concentration of Cs^+ was changed to lower values (3% and 5%) (Figure 5), deviating from the stoichiometric ratio to react with the excessive PbI_2/$PbBr_2$, the crystallization process is still quite different from that without Cs^+. To further understand the influence of the excessive PbI_2/$PbBr_2$, we measured XRD spectra of the as-cast perovskite films without excessive PbI_2/$PbBr_2$, as shown in Figure S9 (Supporting Information). For the film without Cs^+, the residual of 4H and 6H phases can still be clearly identified, indicating that the film still enters stage III. For the film with 10% Cs^+, these secondary phases also disappear, similar to what has been observed for the films with excessive PbI_2/$PbBr_2$. It implies that the reaction of Cs^+ with the excessive PbI_2/$PbBr_2$ may not critically influence the crystallization pathways here.

To understand the relative stability of different phases and the role of Cs doping, we perform DFT calculations to investigate the relative stability of $APbX_3$ phases along the 2H–4H–6H–3C (cubic) pathway (**Figure 6**a). The inherit complexity in this system due to organic cation orientation, multiple mixing components and multiple phases makes it computationally prohibitive to establish a sound baseline for comparing the effect of Cs^+ mixing. Since the $FAPbI_3$ is dominant in the mixed perovskite, we opted for a more simplistic model in one of the limits, the $Cs_xFA_{1-x}PbI_3$, using DFT calculation. For $FAPbI_3$, 2H phase has a lower energy than 4H or 6H phases, the energy difference is larger than 100 meV, and may hinder the formation of 4H, 6H, and subsequently detrimental intermediate phases. When Br substitution is introduced, the overall stability of all phases is enhanced, however, the energy difference between 2H and 4H/6H is lowered (Figure 6a; Figure S10, Supporting Information). Therefore, the combined effect of lower formation energy by ion substitution and entropy contribution from organic cation orientation may have helped driving the 4H–6H–3C phase transition.[29] In addition, we also calculate the concentration dependence of mixing energy in various phases (2H, 4H, 6H, and 3C) of $Cs_xFA_{1-x}PbI_3$ and $Cs_xMA_{1-x}PbBr_3$, as shown in Figure S11 (Supporting Information). The results suggest that the Cs^+ doping could stabilize perovskite phase over 2H, 4H, and 6H phases. The formation energy gain at 12.5% Cs^+ doping concentration (replacing 3 out of 24 FA^+ ion by Cs^+ in 2H, 6H, and 3C phases and 2 out of 16 FA^+ ion in 4H), which is closer to the experimental concentration of 10%, is shown in Figure 6b,

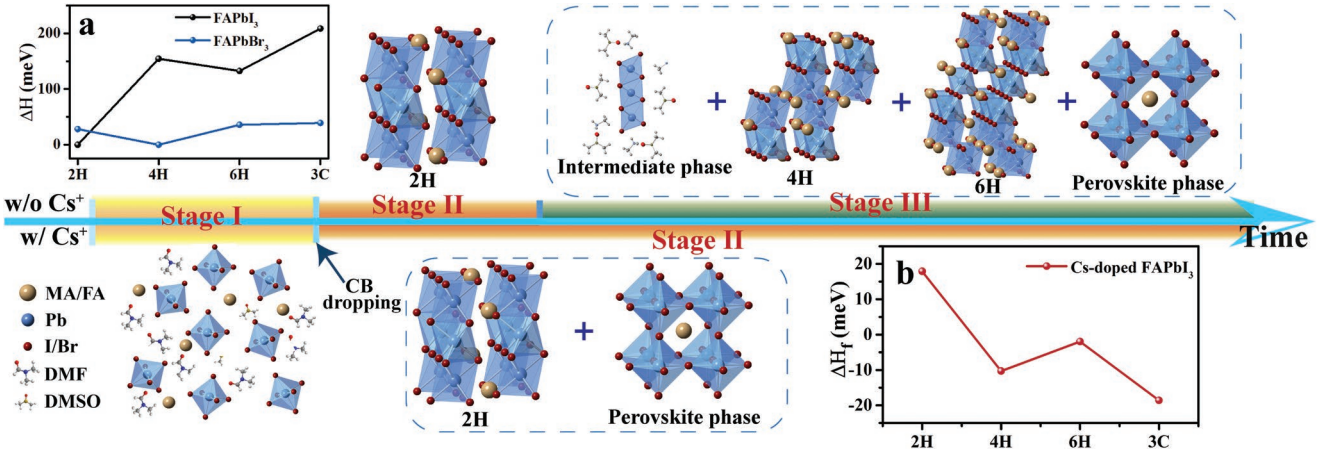

Figure 6. Schematics of phase transition pathways and DFT results. The phase transition pathways of mixed perovskites without and with Cs^+ during the spin-coating operation: a) formation energy (ΔH) of $FAPbI_3$ and $FAPbBr_3$ relative to the most stable structure and b) formation energy gain per formula unit at 12.5% Cs^+ doping relative to undoped case.

© 2019 WILEY-VCH Verlag GmbH & Co. KGaA, Weinheim

indicating that the mixing energy contribution by Cs^+ in favor of formation of perovskite phase relative to 2H, which is consistent with early literature.[30] Noted that the stability of 6H is also enhanced, yet the enhancement is smaller than that of the perovskite phase. A full analysis should include the complexed entropy calculations of different configurations and possible surface or interface effects, which are beyond the scope of this work. Also, note that a proper concentration of Cs replacement is necessary. A higher Cs concentration that corresponds to the experimental limit may lead to further stabilization of perovskite phase. Still, such an enhancement is non-monotonic because a complete replacement of Cs may largely hinder the stability of cubic phases (Figure S10, Supporting Information).

In summary, the crystallization pathways of mixed perovskites $(FAPbI_3)_{0.83}(MAPbBr_3)_{0.17}$ without and with Cs^+ during spinning coating process have been revealed in great detail via in situ GIWAXS (Figure 6). The existence of "annealing window" has been recognized for the first time, which suggests that the as-cast film should be timely annealed within the "annealing window" to achieve a high-quality perovskite film.

For the films without Cs^+, the annealing window is small, in other words, time sensitive. Hexagonal 2H phase forms instantly after the CB dropping. Therefore, it is most likely that the formation of 2H phase overcomes the least energy barriers so as to be observed the earliest. However, it is not stable, quickly transferring to complex phases in stage III. We attribute this to the fundamental crystal structure difference of 2H and its polytypes, which is the ratio of face-sharing and corner-sharing PbX_6 octahedra. It was reported previously that I^- ions favor face-sharing structure while Br^- ions favor corner-sharing structure.[13] Our DFT results further suggest that the phase transition from 2H to 4H, 6H and α-phases is induced by I^- and Br^- ion exchange. A speculative scenario is that 2H phase with pure I^- forms first, followed by partial or pure corner-sharing 4H, 6H and α-phases with mixed I^- and Br^- due to the ion exchange. Concomitantly, the excessive I^- ions generated from the ion exchange promote the formation of MAI–PbI_2–DMSO intermediate phase. Note here, both 2H and MAI–PbI_2–DMSO intermediate phases are not thermally stable, disappeared in the films after thermal annealing at 100 °C. 4H and 6H phases remain in the annealed films, being harmful to the device performance.

For the films with Cs^+, the annealing window is dramatically extended, since the formation of thermally stable 4H and 6H phases are suppressed. Incorporating Cs^+ into the FA-based perovskite is a popular trend recently to achieve high-efficiency devices, mainly attributed to the suppression yellow phase[11] and the reduction of trap density.[31] Its relatively smaller ionic size compared with organic cations could push the tolerance factor toward the appropriate α-phase range. DFT calculations suggest that the incorporation of Cs^+ could lower the formation energy of perovskite phase, consistent with previous studies.[30,32] Moreover, it is evident from our in situ data that the formation starting point of the α-phase moves in accordance with the concentration of Cs^+. The higher the concentration of Cs^+ is, the earlier α-phase appears. It implies that Cs^+ also plays a critical role in the α-phase growth kinetics. More systematic calculations to visualize the full energy landscape change with the Cs^+ doping will facilitate a thorough understanding of the role of Cs^+. In addition, it is worthwhile to further investigate the effect of other alkali metal cations on the perovskite crystallization process such as Rb^+ and K^+ to understand the size and surface passivation effects.

Experimental Section

Materials: $SnCl_2$ (99%) was purchased from Aladdin; methylammonium iodide (MAI), methylammonium bromide (MABr), and formamidinium iodide (FAI) were purchased from Dyesol; lead iodide (99%) and lead bromide (99%) were purchased from TCI; spiro-OMeTAD and FTO glass were purchased from Advanced Election Technology Co., Ltd. All the other chemical materials were purchased from Sigma-Aldrich and used as received unless stated otherwise.

Device Fabrication: FTO substrates were sequentially rinsed by sonication in detergent, deionized (DI) water, acetone and ethanol, and finally dried in air. Then, cleaned FTO substrates were treated with ultraviolet–ozone for 15 min. The colloidal SnO_2 quantum dot (QD) precursor solution was prepared according to the literature.[33] Briefly, $SnCl_2$ and CH_4N_2S with mass ratio of 3:1 were dissolved in 30 mL DI water, then the mixture was stirred for 1–2 d until the solution turned to yellow and clear. A SnO_2 QD electron transporting layer was deposited on FTO substrates by spin-coating the as-prepared colloidal SnO_2 QD solution at 3000 rpm for 40 s, and annealed at 200 °C for 60 min on a hotplate. The perovskite precursor containing 172 mg FAI (1 M), 507 mg PbI_2 (1.1 M), 22.4 mg MABr (0.2 M), and 80.7 mg $PbBr_2$ (0.22 M) in 1 mL anhydrous DMF:DMSO 4:1 (v:v) was prepared according to the literature.[4] Different amount of CsI solution (1.5 M in DMSO) was added to the perovskite precursor to obtain the desired Cs^+ concentration. The perovskite precursor solution was spin coated on substrates following 3 steps: 1000 rpm for 5 s, 6000 rpm for 25 s, and 1500 rpm for 0, 15, 30, or 100 s. During the second step, 160 µL of chlorobenzene was drop-cast on substrates 5 s prior to the end of program. The substrates then were immediately annealed at 100 °C for 1 h. The spiro-OMeTAD solution was composed of 72.3 mg spiro-OMeTAD, 28.8 µL TBP, and 17.5 µL Li-TFSI solution (520 mg in 1 mL acetonitrile) in 1 mL chlorobenzene, and then spin-coated on perovskite film at 4000 rpm for 30 s. Finally, a 50 nm Au electrode was deposited by thermal evaporation.

In Situ GIWAXS Experiments: GIWAXS measurements were conducted at 23A small- and wide-angle X-ray scattering (SWAXS) beamline at the National Synchrotron Radiation Research Center (NSRRC), Hsinchu, Taiwan.[22] The wavelength of X-ray was 1.240 Å (10 keV) and the scattering signals were collected by a C9728DK area detector. The sample to detector distance was ≈166 mm, calibrated with a lanthanum hexaboride (LaB_6) sample. The incident angle was kept at 2° to enhance the signal resolution with a frame exposure time of 3 s. The spin-coating process was conducted in an air-tight chamber under N_2 flow, which consisted of a spin-coater and a motorized syringe for remote injection of CB. After the perovskite precursor was dropped on the substrate, concomitant GIWAXS measurement and sample spinning could be triggered simultaneously, followed by a programmed CB injection on the spinning film at a designated timing during the whole 300 s spinning process at 1500 rpm. There was no visible evidence of X-ray damage on the sample after measurements.

Characterizations: UV–vis absorption spectra were taken on a Hitachi U-3501 ultraviolet/visible/near-infrared spectrophotometer. The current density–voltage (*J–V*) curves were measured by a Keithley 2400 source meter unit under an AM 1.5G solar simulator (100 mW cm^{-2}). The devices were measured without pretest illumination and bias poling, and the scan rate is 0.2 V s^{-1}. Morphologies of the perovskite films were observed by high-resolution field emission scanning electron microscopy (HR-FESEM) (FEI, Quanta 400). The crystalline structures for the perovskite films were characterized by X-ray diffraction (Rigaku, Smart Lab).

DFT Calculations: Density functional theory calculation is performed within the generalized gradient approximation using the Perdew–Burke–Ernzerhof exchange correlation functional[34] as implemented in the Vienna

© 2019 WILEY-VCH Verlag GmbH & Co. KGaA, Weinheim

Ab Initio Simulation Package (VASP)[35] without including spin-orbit coupling. Ground state energy of 2H, 4H, and 6H phases is calculated using the hexagonal unit cell, with reciprocal space sampling $\geq 3 \times 3 \times 3$ for one 2H unit cell including Γ-point. The orientation of organic cations cannot be significantly rotated by relaxation alone, similar conclusion is also found in previous work concerning cubic perovskite.[29] In this work, simulated annealing is performed from several initial orientations, followed by structural relaxation until Hellmann–Feynman force is less than 0.01 eV $Å^{-1}$, and the lowest energy is reported. The formation energy of ABX_3 is defined as ΔH_f ($APbX_3$) = E($APbX_3$) − E(AX) − E(PbX_2).

Supporting Information

Supporting Information is available from the Wiley Online Library or from the author.

Acknowledgements

The authors are grateful for the beam time and technical support provided by 23A SWAXS beamline at NSRRC, Hsinchu. The authors acknowledge the financial support from Research Grant Council of Hong Kong (RGC) (General Research Fund No. 14314216) and CUHK Direct Grant (No. 4441636).

Conflict of Interest

The authors declare no conflict of interest.

Keywords

annealing window, crystallization pathways, Cs doping, in situ GIWAXS, perovskite solar cells

Received: February 25, 2019
Revised: March 31, 2019
Published online: April 30, 2019

[1] a) J. Wang, N. Wang, Y. Jin, J. Si, Z. K. Tan, H. Du, L. Cheng, X. Dai, S. Bai, H. He, Z. Ye, M. L. Lai, R. H. Friend, W. Huang, *Adv. Mater.* **2015**, *27*, 2311; b) S. Zhang, C. Yi, N. Wang, Y. Sun, W. Zou, Y. Wei, Y. Cao, Y. Miao, R. Li, Y. Yin, N. Zhao, J. Wang, W. Huang, *Adv. Mater.* **2017**, *29*, 1606600; c) X. Yang, X. Zhang, J. Deng, Z. Chu, Q. Jiang, J. Meng, P. Wang, L. Zhang, Z. Yin, J. You, *Nat. Commun.* **2018**, *9*, 570; d) J. Xing, Y. Zhao, M. Askerka, L. N. Quan, X. Gong, W. Zhao, J. Zhao, H. Tan, G. Long, L. Gao, Z. Yang, O. Voznyy, J. Tang, Z. H. Lu, Q. Xiong, E. H. Sargent, *Nat. Commun.* **2018**, *9*, 3541.

[2] a) J.-W. Xiao, L. Liu, D. Zhang, N. De Marco, J.-W. Lee, O. Lin, Q. Chen, Y. Yang, *Adv. Energy Mater.* **2017**, *7*, 1700491; b) M. S. Juan-Pablo Correa-Baena, T. Buonassisi, M. Grätzel, A. Abate, W. Tress, A. Hagfeldt, *Science* **2017**, *358*, 739; c) J.-P. Correa-Baena, A. Abate, M. Saliba, W. Tress, T. Jesper Jacobsson, M. Grätzel, A. Hagfeldt, *Energy Environ. Sci.* **2017**, *10*, 710.

[3] a) A. Kojima, K. Teshima, Y. Shirai, T. Miyasaka, *J. Am. Chem. Soc.* **2009**, *131*, 6050; b) J. H. Heo, S. H. Im, J. H. Noh, T. N. Mandal, C.-S. Lim, J. A. Chang, Y. H. Lee, H.-j. Kim, A. Sarkar, M. K. Nazeeruddin, M. Grätzel, S. I. Seok, *Nat. Photonics* **2013**, *7*, 486; c) Q. F. Dong, Y. J. Fang, Y. C. Shao, P. Mulligan, J. Qiu, L. Cao, J. S. Huang, *Science* **2015**, *347*, 967; d) H. P. Zhou, Q. Chen, G. Li, S. Luo, T. B. Song, H. S. Duan, Z. R. Hong, J. B. You, Y. S. Liu, Y. Yang, *Science* **2014**, *345*, 542; e) J. H. Im, C. R. Lee, J. W. Lee, S. W. Park, N. G. Park, *Nanoscale* **2011**, *3*, 4088.

[4] M. Saliba, T. Matsui, K. Domanski, J. Y. Seo, A. Ummadisingu, S. M. Zakeeruddin, J. P. Correa-Baena, W. R. Tress, A. Abate, A. Hagfeldt, M. Gratzel, *Science* **2016**, *354*, 206.

[5] a) G. Kieslich, S. Sun, A. K. Cheetham, *Chem. Sci.* **2014**, *5*, 4712; b) M. R. Filip, G. E. Eperon, H. J. Snaith, F. Giustino, *Nat. Commun.* **2014**, *5*, 5757; c) V. M. Goldschmidt, *Naturwissenschaften* **1926**, *14*, 477.

[6] J. H. Im, I. H. Jang, N. Pellet, M. Gratzel, N. G. Park, *Nat. Nanotechnol.* **2014**, *9*, 927.

[7] J. W. Lee, D. J. Seol, A. N. Cho, N. G. Park, *Adv. Mater.* **2014**, *26*, 4991.

[8] G. E. Eperon, G. M. Paternò, R. J. Sutton, A. Zampetti, A. A. Haghighirad, F. Cacialli, H. J. Snaith, *J. Mater. Chem. A* **2015**, *3*, 19688.

[9] N. J. Jeon, J. H. Noh, W. S. Yang, Y. C. Kim, S. Ryu, J. Seo, S. I. Seok, *Nature* **2015**, *517*, 476.

[10] W. Rehman, D. P. McMeekin, J. B. Patel, R. L. Milot, M. B. Johnston, H. J. Snaith, L. M. Herz, *Energy Environ. Sci.* **2017**, *10*, 361.

[11] M. Saliba, T. Matsui, J. Y. Seo, K. Domanski, J. P. Correa-Baena, M. K. Nazeeruddin, S. M. Zakeeruddin, W. Tress, A. Abate, A. Hagfeldt, M. Gratzel, *Energy Environ. Sci.* **2016**, *9*, 1989.

[12] a) T. Wang, F. Xu, Y. Li, Y. Zhao, *Sol. RRL* **2018**, *2*, 1700180; b) Y. Wang, T. Zhang, M. Kan, Y. Zhao, *J. Am. Chem. Soc.* **2018**, *140*, 12345.

[13] P. Gratia, I. Zimmermann, P. Schouwink, J.-H. Yum, J.-N. Audinot, K. Sivula, T. Wirtz, M. K. Nazeeruddin, *ACS Energy Lett.* **2017**, *2*, 2686.

[14] M. Saliba, J.-P. Correa-Baena, C. M. Wolff, M. Stolterfoht, N. Phung, S. Albrecht, D. Neher, A. Abate, *Chem. Mater.* **2018**, *30*, 4193.

[15] a) K. Meng, L. Wu, Z. Liu, X. Wang, Q. Xu, Y. Hu, S. He, X. Li, T. Li, G. Chen, *Adv. Mater.* **2018**, *30*, 1706401; b) H. C. Chia, H. S. Sheu, Y. Y. Hsiao, S. S. Li, Y. K. Lan, C. Y. Lin, J. W. Chang, Y. C. Kuo, C. H. Chen, S. C. Weng, C. J. Su, A. C. Su, C. W. Chen, U. S. Jeng, *ACS Appl. Mater. Interfaces* **2017**, *9*, 36897; c) M. Long, T. Zhang, M. Liu, Z. Chen, C. Wang, W. Xie, F. Xie, J. Chen, G. Li, J. Xu, *Adv. Mater.* **2018**, *30*, 1801562.

[16] V. L. Pool, B. Dou, D. G. Van Campen, T. R. Klein-Stockert, F. S. Barnes, S. E. Shaheen, M. I. Ahmad, M. F. van Hest, M. F. Toney, *Nat. Commun.* **2017**, *8*, 14075.

[17] M. Alsari, O. Bikondoa, J. Bishop, M. Abdi-Jalebi, L. Y. Ozer, M. Hampton, P. Thompson, M. T. Hörantner, S. Mahesh, C. Greenland, J. E. Macdonald, G. Palmisano, H. J. Snaith, D. G. Lidzey, S. D. Stranks, R. H. Friend, S. Lilliu, *Energy Environ. Sci.* **2018**, *11*, 383.

[18] R. Munir, A. D. Sheikh, M. Abdelsamie, H. Hu, L. Yu, K. Zhao, T. Kim, O. E. Tall, R. Li, D. M. Smilgies, A. Amassian, *Adv. Mater.* **2017**, *29*, 1604113.

[19] Q. Hu, L. Zhao, J. Wu, K. Gao, D. Luo, Y. Jiang, Z. Zhang, C. Zhu, E. Schaible, A. Hexemer, C. Wang, Y. Liu, W. Zhang, M. Gratzel, F. Liu, T. P. Russell, R. Zhu, Q. Gong, *Nat. Commun.* **2017**, *8*, 15688.

[20] Y. Zhong, R. Munir, J. Li, M.-C. Tang, M. R. Niazi, D.-M. Smilgies, K. Zhao, A. Amassian, *ACS Energy Lett.* **2018**, *3*, 1078.

[21] T. Jesper Jacobsson, J.-P. Correa-Baena, M. Pazoki, M. Saliba, K. Schenk, M. Grätzel, A. Hagfeldt, *Energy Environ. Sci.* **2016**, *9*, 1706.

[22] W.-R. Wu, C.-J. Su, W.-T. Chuang, Y.-C. Huang, P.-W. Yang, P.-C. Lin, C.-Y. Chen, T.-Y. Yang, A.-C. Su, K.-H. Wei, C.-M. Liu, U. S. Jeng, *Adv. Energy Mater.* **2017**, *7*, 1601842.

[23] M. Konstantakou, D. Perganti, P. Falaras, T. Stergiopoulos, *Crystals* **2017**, *7*, 291.

 © 2019 WILEY-VCH Verlag GmbH & Co. KGaA, Weinheim

[24] N. J. Jeon, J. H. Noh, Y. C. Kim, W. S. Yang, S. Ryu, S. I. Seok, *Nat. Mater.* **2014**, *13*, 897.
[25] M. Qin, J. Cao, T. Zhang, J. Mai, T.-K. Lau, S. Zhou, Y. Zhou, J. Wang, Y.-J. Hsu, N. Zhao, J. Xu, X. Zhan, X. Lu, *Adv. Energy Mater.* **2018**, *8*, 1703399.
[26] W. S. Yang, B. W. Park, E. H. Jung, N. J. Jeon, Y. C. Kim, D. U. Lee, S. S. Shin, J. Seo, E. K. Kim, J. H. Noh, S. I. Seok, *Science* **2017**, *356*, 1376.
[27] J. Cao, X. Jing, J. Yan, C. Hu, R. Chen, J. Yin, J. Li, N. Zheng, *J. Am. Chem. Soc.* **2016**, *138*, 9919.
[28] B. W. Park, N. Kedem, M. Kulbak, D. Y. Lee, W. S. Yang, N. J. Jeon, J. Seo, G. Kim, K. J. Kim, T. J. Shin, G. Hodes, D. Cahen, S. I. Seok, *Nat. Commun.* **2018**, *9*, 3301.
[29] T. Chen, B. J. Foley, C. Park, C. M. Brown, L. W. Harriger, J. Lee, J. Ruff, M. Yoon, J. J. Choi, S.-H. Lee, *Sci. Adv.* **2016**, *2*, e1601650.
[30] C. Yi, J. Luo, S. Meloni, A. Boziki, N. Ashari-Astani, C. Grätzel, S. M. Zakeeruddin, U. Röthlisberger, M. Grätzel, *Energy Environ. Sci.* **2016**, *9*, 656.
[31] Y. Hu, E. M. Hutter, P. Rieder, I. Grill, J. Hanisch, M. F. Aygüler, A. G. Hufnagel, M. Handloser, T. Bein, A. Hartschuh, K. Tvingstedt, V. Dyakonov, A. Baumann, T. J. Savenije, M. L. Petrus, P. Docampo, *Adv. Energy Mater.* **2018**, *8*, 1703057.
[32] J. Cao, S. X. Tao, P. A. Bobbert, C. P. Wong, N. Zhao, *Adv. Mater.* **2018**, *30*, 1707350.
[33] G. Yang, C. Chen, F. Yao, Z. Chen, Q. Zhang, X. Zheng, J. Ma, H. Lei, P. Qin, L. Xiong, W. Ke, G. Li, Y. Yan, G. Fang, *Adv. Mater.* **2018**, *30*, 1706023.
[34] J. Perdew, K. Burke, M. Ernzerhof, *Phys. Rev. Lett.* **1996**, *77*, 3865.
[35] G. Kresse, J. Furthmuller, *Phys. Rev. B* **1996**, *54*, 11169.

 © 2019 WILEY-VCH Verlag GmbH & Co. KGaA, Weinheim